ACSNANO

www.acsnano.org

ARTICLE

Atomically Dispersed Iron–Nitrogen Sites on Hierarchically Mesoporous Carbon Nanotube and Graphene Nanoribbon Networks for CO_2 Reduction

Fuping Pan, Boyang Li, Erik Sarnello, Yuhuan Fei, Yang Gang, Xianmei Xiang, Zichen Du, Peng Zhang, Guofeng Wang, Hoai T. Nguyen, Tao Li, Yun Hang Hu, Hong-Cai Zhou, and Ying Li*

Cite This: *ACS Nano* 2020, 14, 5506–5516

Read Online

ACCESS | Metrics & More | Article Recommendations | Supporting Information

ABSTRACT: **Atomically dispersed metal and nitrogen co-doped carbon (M-N/C) catalysts hold great promise for electrochemical CO_2 conversion. However, there is a lack of cost-effective synthesis approaches to meet the goal of economic mass production of single-atom M-N/C with desirable carbon support architecture for efficient CO_2 reduction. Herein, we report facile transformation of commercial carbon nanotube (CNT) into isolated Fe–N_4 sites anchored on carbon nanotube and graphene nanoribbon (GNR) networks (Fe-N/CNT@GNR). The oxidization-induced partial unzipping of CNT results in the generation of GNR nanolayers attached to the remaining fibrous CNT frameworks, which reticulates a hierarchically mesoporous complex and thus enables a high electrochemical active surface area and smooth mass transport. The Fe residues originating from CNT growth seeds serve as Fe sources to form isolated Fe–N_4 moieties located at the CNT and GNR basal plane and edges with high intrinsic capability of activating CO_2 and suppressing hydrogen evolution. The Fe-N/CNT@GNR delivers a stable CO Faradaic efficiency of 96% with a partial current density of 22.6 mA cm^{-2} at a low overpotential of 650 mV, making it one of the most active M-N/C catalysts reported. This work presents an effective strategy to fabricate advanced atomistic catalysts and highlights the key roles of support architecture in single-atom electrocatalysis.**

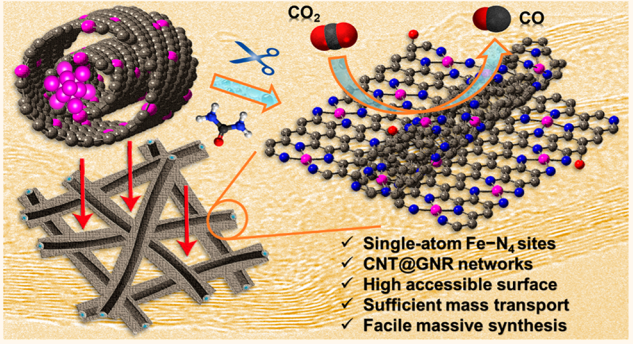

KEYWORDS: *single-atom catalyst, carbon architecture, nanotubes, nanoribbons, CO_2 reduction*

The increasing emissions of CO_2 from the consumption of fossil fuel have caused concerns on global climate change and motivated the development of clean energy technologies. Electrochemical CO_2 conversion into value-added fuels or chemicals under ambient conditions presents a promising approach to mitigate net CO_2 emissions and alleviate the dependence on petrochemicals to meet the energy demand.[1,2] However, CO_2 reduction reaction (CO_2RR) suffers from not only the sluggish kinetics, sophisticated reaction pathways with uncontrolled product selectivity, but also inevitable competition over the hydrogen evolution reaction (HER).[1,3−5] These limitations hinder the industrial application of CO_2 electrolysis, which is thus eventually contingent upon the development of highly active and selective CO_2RR electrocatalysts. Currently, noble metals Au and Ag are state-of-the-art CO_2RR catalysts with high CO_2-to-CO selectivity but have the inherent drawbacks of prohibitive cost and scarcity.[6,7]

Extensive efforts have been devoted to developing efficient electrocatalysts made of earth-abundant elements for CO_2RR, especially atomically dispersed metal and nitrogen co-doped carbon (M-N/C) catalysts.[8−16] By virtue of maximum atom utilization and unfavorable hydrogen chemisorption on single-atom metals coordinated with nitrogen (M–N_x) sites,[8−14,17,18] M-N/C holds great promise to maximize the efficiency and

Received: December 8, 2019
Accepted: April 24, 2020
Published: April 24, 2020

https://dx.doi.org/10.1021/acsnano.9b09658
ACS Nano 2020, 14, 5506–5516

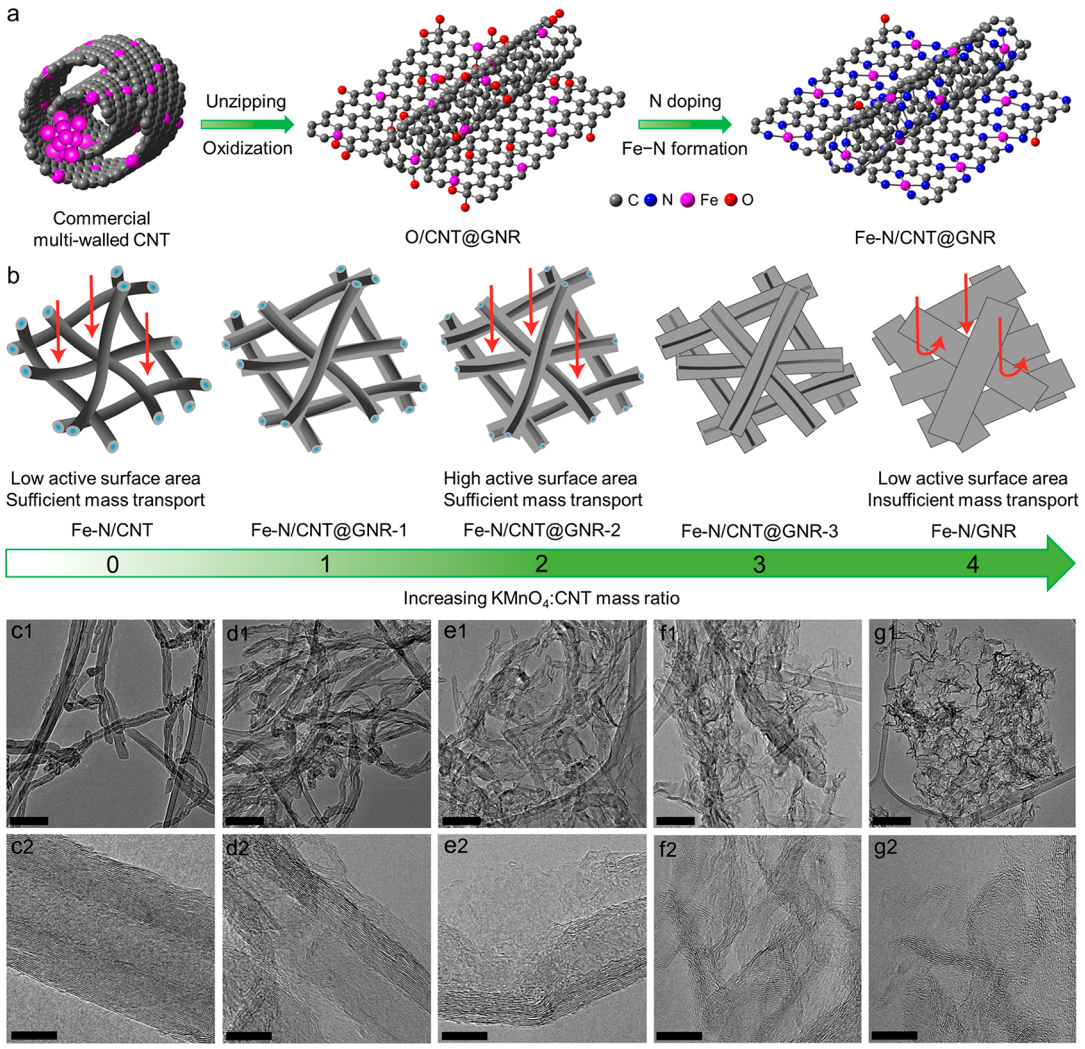

Figure 1. (a) Schematic illustration of transforming multiwalled CNTs into Fe-N/CNT@GNR. (b) Structural evolution from CNTs to CNT@GNR to GNR by adjusting $KMnO_4$:CNT mass ratios. TEM images for Fe-N/CNT (c), Fe-N/CNT@GNR-1 (d), Fe-N/CNT@GNR-2 (e), Fe-N/CNT@GNR-3 (f), and Fe-N/GNR (g). Scale bar in c1−g1 is 100 nm, and scale bar in c2−g2 is 10 nm.

selectivity for CO_2 reduction while suppressing undesired HER. Previous approaches to prepare isolated M-N/C include atomic layer deposition,[19] carbonization of doped metal−organic frameworks (MOFs),[9,20,21] adsorption-assisted surface immobilization,[10,22,23] and confined pyrolysis strategy.[24,25] However, these methods either face difficulty in scaling up or involve multistep complicated processes and use of expensive precursors, making them impractical for mass production. The challenges drive the exploration of simple and economic methods to fabricate monodispersed M-N/C for the large-scale commercialization of CO_2 electrolysis.

Besides the synthesis of isolated M−N_x moieties, the architecture of carbon supports also plays a key role in governing the performance of M-N/C, as it determines the accessibility of active sites and mass transport.[26] Graphene and carbon nanotubes are the most extensively used supports in M-N/C for electrochemical reactions. Although traditional graphene-based M-N/C could provide dense M−N_x sites throughout the carbon layer, the electrochemical active area at the gas/solid/liquid three-phase interface is commonly insufficient because two-dimensional (2D) ultrathin graphene nanosheets easily tend to stack due to the strong $\pi-\pi$ interaction between interlayers.[27] The agglomeration also results in poor mass delivery owing to the lack of porous channels.[28] Using carbon nanotubes can afford highly porous networks to enable efficient mass transfer.[29,30] The key drawback, however, is the low density of available M−N_x sites since only the M−N_x anchored on the outermost walls are believed to be able to reach reactants, while the M−N_x confined in the inner walls of carbon nanotubes is not accessible for reactions. Thus, there is a considerable need in developing facile, cost-effective, and scalable approaches to fabricate M-N/C with favorable carbon architecture decorated with atomically dispersed M−N_x sites to enable high-efficiency CO_2 reduction.

Herein, we report a facile and massive synthesis of single-atom iron catalysts to drive CO_2 reduction through transforming commercial carbon nanotubes into atomically dispersed Fe−N_4 sites supported on hierarchical carbon nanotube (CNT) and graphene nanoribbon (GNR) networks (Fe-N/CNT@GNR). We selected commercially available multiwalled CNTs prepared by catalytic chemical vapor deposition as the starting materials, in which Fe residues can be directly used to grow Fe−N_4 species without adding a supernumerary Fe source. The chemical unzipping of the CNTs generates the GNR nanolayers intimately attached on the outer walls of the CNTs, and the subsequent N doping leads to the formation of atomically

https://dx.doi.org/10.1021/acsnano.9b09658
ACS Nano 2020, 14, 5506−5516

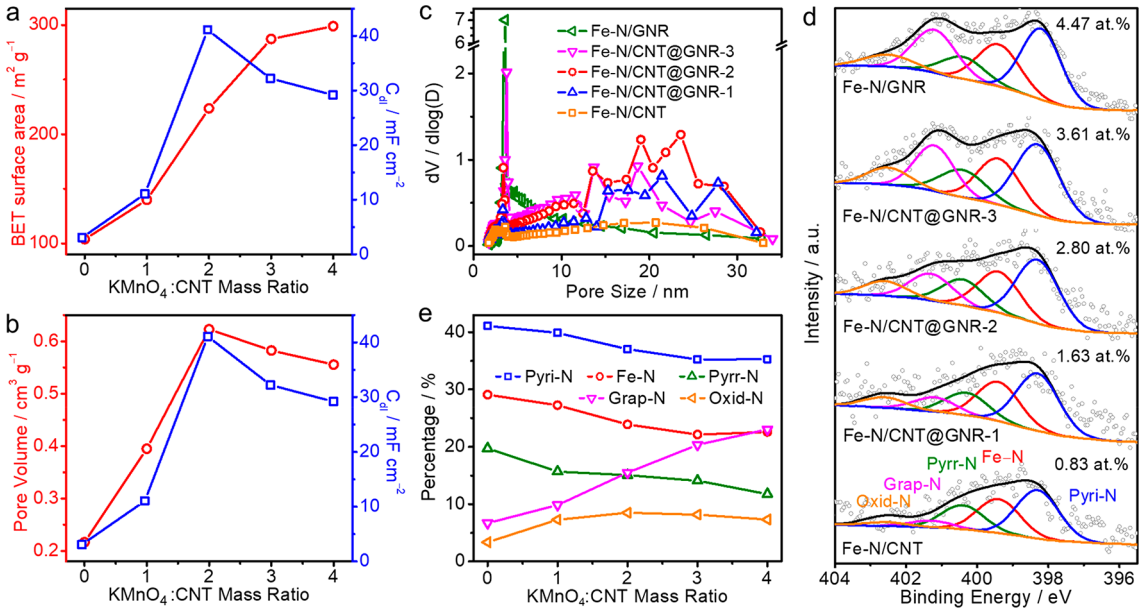

Figure 2. (a) BET surface area, (b) pore volumes, (c) pore size distribution, (d) N 1s XPS spectra, and (e) percentages of N species for Fe-N/CNT, Fe-N/CNT@GNR, and Fe-N/GNR.

dispersed Fe coordinated with N (Fe−N_4). In this architecture, the CNTs act as a fibrous skeleton to anchor the GNRs and hinder their aggregation, which also forms the mesoporous channels for smooth mass diffusion. The hybrid structure enables the hosting of monodispersed Fe−N_4 on the CNT and GNR basal plane and edges as accessible active and selective centers to boost CO_2 activation and suppress HER, as revealed by density functional theory (DFT) computations. By virtue of these favorable carbon support structures and the high intrinsic reactivity of isolated Fe sites, Fe-N/CNT@GNR exhibited enhanced performance for the reduction of CO_2 to CO, which is placed at the top level among M-N/C catalysts reported.

RESULTS AND DISCUSSION

To synthesize Fe-N/CNT@GNR, the CNTs were first oxidized in a $KMnO_4/H_2SO_4$ solution, during which the CNTs were unzipped longitudinally owing to the weakening and breaking of C−C bonds by oxygen-group-created defects (Figure 1a),[31−33] leading to the formation of O/CNT@GNR with Fe impurities (Figures S1−S3). The subsequent N doping *via* heating O/CNT@GNR with urea resulted in the final Fe-N/CNT@GNR catalyst. We found that 900 °C was the optimal heating temperature to obtain the best catalyst for CO_2 reduction (Figure S4). The structure evolution from CNT to CNT@GNR and GNR can be readily controlled (Figure 1b). Specifically, the CNTs cannot be unzipped without adding $KMnO_4$ (Figure S2), and the catalyst was labeled as Fe-N/CNT. The unzipping of CNTs occurs with the addition of $KMnO_4$ as oxidant, and the degree of consecutive tube opening can be tuned by adjusting the amount of $KMnO_4$. The corresponding catalysts were denoted as Fe-N/CNT@GNR-*x*, where *x* refers to the mass ratio of $KMnO_4$:CNT and varies from 1 to 3. When *x* was increased to 4, the CNTs were completely converted into the GNRs, with the catalyst being named as Fe-N/GNR. Using this approach, we can achieve the gram-scale synthesis of atomic Fe-N/CNT@GNR (Figure S5). It is expected that the synthesis can be further scaled to the industry level utilizing large-size utensils and mechanical equipment, such as ball milling to mix urea with O/CNT@GNR.

Transmission electron microscope (TEM) images show the structural evolution during the oxidizing process. Compared to the tubular feature of Fe-N/CNT (Figure 1c), Fe-N/CNT@GNR exhibited ribbon-like graphene nanosheets with an interlayer distance of 0.34 nm closely attached on the remaining CNTs backbones (Figure 1d−f). The size of the GNRs gradually becomes larger with increasing $KMnO_4$ amount, whereas the diameter of the remaining CNTs decreases (Figure S6). In the case of Fe-N/GNR, CNTs were fully unzipped, displaying a typical few-layer graphene feature without any residual CNT (Figure 1g). The damage of multiwalled CNTs can be further monitored from the decreased intensity of the (002) peak at 26° in the X-ray diffraction (XRD) patterns (Figure S7), suggesting a gradually disordered arrangement of carbon layers from the CNT matrix to exfoliated GNRs. On the other hand, the metallic Fe and Fe_3C exist in Fe-N/CNT but disappear in Fe-N/CNT@GNR and Fe-N/GNR. This can be attributed to the structure disruption of CNTs caused by the strong oxidization, which enhances the exposure of Fe-based particle residues to the acid solution and thus facilitates their elimination.

N_2 adsorption−desorption analyses reveal that the Brunauer−Emmett−Teller (BET) surface area gradually increases from 104 $m^2 g^{-1}$ on Fe-N/CNT to 224 $m^2 g^{-1}$ on Fe-N/CNT@GNR-2 and 299 $m^2 g^{-1}$ on Fe-N/GNR (Figure 2a), which can be ascribed to the generation of external graphitic nanosheets. In addition, we found the pore volume first increases from 0.22 $cm^3 g^{-1}$ on Fe-N/CNT to 0.62 $cm^3 g^{-1}$ on Fe-N/CNT@GNR-2 and then decreases to 0.55 $cm^3 g^{-1}$ on Fe-N/GNR (Figure 2b). The pore distribution clearly demonstrates that large mesopores at around 10−30 nm were formed in Fe-N/CNT@GNR, which, however, were not observed in Fe-N/CNT and Fe-N/GNR (Figure 2c). These observations confirm the evolution of large-size mesopores in the CNT@GNR complex by coupling CNTs with GNRs, and the disappearance of mesopores in Fe-N/GNR might be as a consequence of the stacking of GNRs due to the loss of CNT mainstays as spacers (Figure 1b). We further

https://dx.doi.org/10.1021/acsnano.9b09658
ACS Nano 2020, 14, 5506−5516

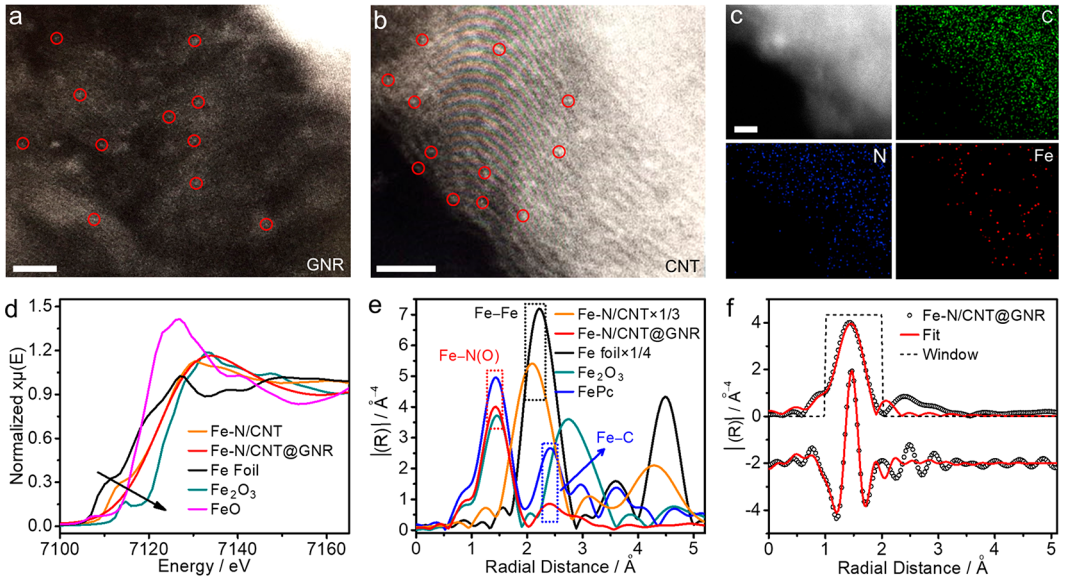

Figure 3. (a, b) HAADF-STEM and (c) elemental mapping images of Fe-N/CNT@GNR-2. Scale bars in a, b, and c are 2 nm. (d) XANES and (e) Fourier transformation of the EXAFS spectra of Fe-N/CNT, Fe-N/CNT@GNR-2, and standard references. (f) Fitting of Fourier transformations of EXAFS spectra for Fe-N/CNT@GNR-2 including magnitude (top) and imaginary (bottom) parts.

measured double-layer capacity (C_{dl}) at the electrode/electrolyte interface (Figure S8), which refers to electrochemical active surface areas (ECSA).[34] We found that the C_{dl} shows a similar increasing tendency with the pore volume and BET surface area when the $KMnO_4$:CNT mass ratio is lower than 3 (Figure 2a,b); however, the C_{dl} decreases accompanied by the decline in pore volume when the $KMnO_4$:CNT mass ratio is larger than 3, despite the surface area still increasing. The results indicate that the mesopores significantly contribute to the increase in the effective active area at the interface of the solid catalyst and liquid electrolyte, which can be explained by Sung's discovery that the mesopores serve as channels for the reaction medium to electrolyte wetting of the catalyst surface.[35] Accordingly, Fe-N/CNT@GNR-2 exhibited a larger C_{dl} than Fe-N/CNT and Fe-N/GNR, making it a promising architecture with enhanced accessibility of surface sites for electrocatalytic reactions.

The surface N content, measured by X-ray photoelectron spectroscopy (XPS), presents a positive linear tendency as a function of C−O:C ratio in O/CNT@GNR, increasing from 0.86 at. % on Fe-N/CNT to 2.80 at. % on Fe-N/CNT@GNR-2 and to 4.47 at. % on Fe-N/GNR (Figure S9, Table S1). This implies that the N doping process underwent a reaction between N-containing reactive gases from urea thermolysis and C−O/C═O groups on O/CNT@GNR (Figure S10).[36] By deconvoluting N 1s spectra (Figure 2d), five kinds of N species can be identified, including pyridinic N (398.2 eV), Fe−N (399.5 eV), pyrrolic N (400.3 eV), graphitic N (401.2 eV), and N-oxides (403.7 eV).[23,37−39] Notably, the percentages of the edge-located pyridinic N and pyrrolic N gradually decrease upon increasing of the opening degree of the CNT,[40] whereas the portion of the bulk-hosted graphitic N increases (Figure 2e). This tendency further confirms the exposure of more graphene basal plane with the increase in the tearing of CNTs by introducing more $KMnO_4$, supporting the TEM observation (Figure 1c−g) that the CNT is controllably unzipped into CNT@GNR and finally GNR by adjusting the $KMnO_4$ amount.

The isolated dispersion of Fe atoms was revealed by high-angle annular dark-field aberration-corrected scanning transmission electron microscopy (HAADF-STEM). As shown in Figure 3a,b, bright dots corresponding to Fe atoms dispersed throughout GNRs and CNTs were clearly observed. The elemental mapping images demonstrate the dense distribution of N, while Fe is sparsely dispersed (Figure 3c), consistent with the STEM images. To unravel the local arrangements of Fe atoms, X-ray absorption spectroscopy (XAS) was performed on Fe-N/CNT and Fe-N/CNT@GNR-2, in which Fe foil, Fe_2O_3, FeO, and iron phthalocyanine (FePc) were used as standard references. As shown in X-ray absorption near edge structure (XANES) spectra (Figure 3d), the adsorption edge profile (line position) of Fe-N/CNT is in between Fe foil and FeO. This suggests that Fe may have an oxidization state between 0 and 2+, probably due to the formation of Fe_3C, in agreement with the XRD observation. As for Fe-N/CNT@GNR-2, the edge-position profile is situated between Fe foil and Fe_2O_3 but much closer to FeO; thus it is more likely that the Fe atoms have a positive charge dominantly at 2+.[41] Note that the presence of both 2+ and 3+ in Fe 2p XPS spectra might be due to the surface oxidization when the catalyst was exposed to air (Figure S11), and no other metals (*e.g.*, Co, Ni, and Mn) were detected. Furthermore, extended X-ray absorption fine structure (EXAFS) was analyzed to uncover the coordination environment of Fe atoms. As depicted in Figure 3e and Figure S12, Fe-N/CNT showed an obvious peak at 2.1 Å, which is assigned to the Fe−Fe bond. Notably, Fe-N/CNT@GNR-2 exhibited a single peak at 1.45 Å, which corresponds to the bond length of Fe−N in FePc and Fe−O in Fe_2O_3. Note that there is a minor peak around 2.5 Å in Fe-N/CNT@GNR-2, which is similar to the standard reference FePc and can be attributed to the backscattering from carbon atoms.[42] The absence of the Fe−Fe signal further verifies the monodispersed nature of Fe atoms in Fe-N/CNT@GNR-2.

We further fitted EXAFS to obtain quantitative structural parameters of Fe (Figure 3f). The best-fitting results show that the coordination number of Fe is five with a bond length of 1.97 Å in Fe-N/CNT@GNR-2 (Table S2). According to the previous structural identification in the literature,[43,44] it is more likely that one Fe atom bonds with four N atoms in the carbon matrix and one end-on adsorbed oxygen molecule. The

https://dx.doi.org/10.1021/acsnano.9b09658
ACS Nano 2020, 14, 5506−5516

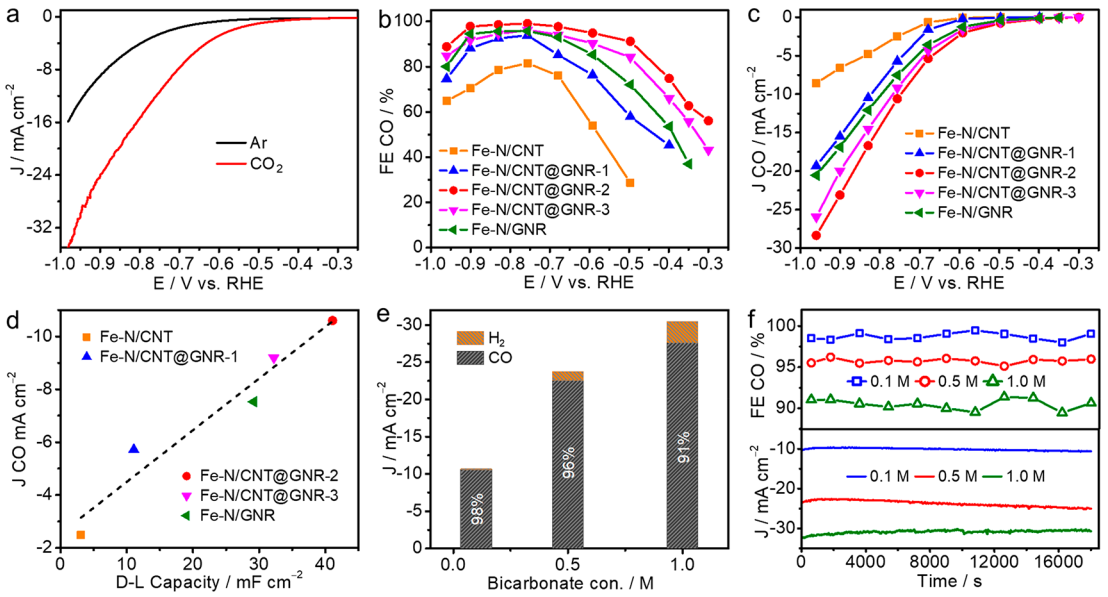

Figure 4. (a) LSV curves acquired in Ar- and CO_2-saturated 0.1 M $KHCO_3$. (b) CO Faradaic efficiency and (c) CO partial current density on various catalysts in 0.1 M $KHCO_3$. (d) Correlation between CO partial current density and double-layer capacity. (e) Current density and CO Faradaic efficiency in 0.1, 0.5, and 1.0 M $KHCO_3$ solution at −0.76 V. (f) Stability in the various electrolyte conditions at −0.76 V.

actual Fe content, detected by inductively coupled plasma mass spectrometry (ICP-MS), is 6.98 wt % in Fe-N/CNT, which decreases to 1.75 wt % in Fe-N/CNT@GNR-2 and 1.72 wt % in Fe-N/GNR due to the loss of Fe-based aggregates. Note that the surface Fe content on Fe-N/CNT is lower compared to others (Table S1), which, however, almost remains at the same level when $KMnO_4$ was used to unzip CNTs. This highlights the critical role of the strong oxidization process in leaching Fe particles and forming the uniform dispersion of Fe atoms throughout the surface of catalysts.

The electrocatalytic CO_2RR properties were evaluated in a three-electrode H-cell. The identification of reaction products after stable electrolysis shows that CO and H_2 are detectable gaseous species by gas chromatography (GC), accounting for a total Faradaic efficiency (FE) around 99% (Figure S13, Figure S14); no C_2 products (such as ethylene, ethanol, acetic acid) were observed by both GC and ^{1}H NMR (Figure S15). This phenomenon is consistent with the reported findings that CO is the dominant product on single-atom Fe−N sites (Table S3).[45,46] In the CO_2RR process, it has been widely accepted that the pathway to C_2 products undergoes the formation of an adsorbed *CO intermediate and the subsequent C−C coupling *via* the dimerization of *CO, as observed on copper-based metals and oxide catalysts.[47,48] In the case of a single-atom Fe−N site, despite that adsorbed *CO can be generated, it cannot catalyze CO dimerization to form a C−C bond, thus leading to the formation of CO as the main final product.

In comparison to linear sweep voltammetry (LSV) curves recorded in the Ar-saturated 0.1 M $KHCO_3$ solution, the significant increase in current density in the CO_2-saturated solution suggests the occurrence of CO_2 reduction (Figure 4a). The CO FEs at different potentials are depicted in Figure 4b and Figure S16, showing good repeatability. Fe-N/CNT@GNR-2 showed CO FEs above 90% at a wide potential range of −0.5 to −0.95 V; the highest FE of 98% was achieved at −0.76 V. In contrast, Fe-N/CNT and Fe-N/GNR exhibited the maximum CO FEs of 82% and 92%, respectively, at −0.76 V, lower than that of Fe-N/CNT@GNR-2. Furthermore, the CO partial currents are highly dependent on the structure of the catalysts, following the order Fe-N/CNT < Fe-N/CNT@GNR-1 < Fe-N/GNR < Fe-N/CNT@GNR-3 < Fe-N/CNT@GNR-2 (Figure 4c). The best-performing Fe-N/CNT@GNR-2 delivered CO currents from 0.1 to 28.3 mA cm^{-2} in the potential range from −0.3 to −0.96 V. When plotting CO currents as a function of C_{dl} for various catalysts, it shows a roughly linear relationship (Figure 4d). This demonstrates that the integrated architecture of the CNT and GNR complex supplies more available Fe sites for CO_2 reduction than the CNT and GNR supports, as evidenced by the structure-dependent active surface area (Figure 2a,b). Tafel plot analyses present that all catalysts possessed similar Tafel slopes around 118 mV dec^{-1} (Figure S17), implying that the reduction of CO_2 to CO proceeds through the formation of COOH* as the rate-limiting step.[23]

We further tested CO_2RR activity in varied concentrations of $KHCO_3$ electrolytes. As shown in Figure 4e and Figure S18, the maximum CO FE decreases from 98% to 96% and 91% in the 0.1, 0.5, and 1 M $KHCO_3$ solutions at −0.76 V, while the corresponding total current density increases from 10.7 to 23.8 and 30.5 mA cm^{-2}, respectively. This demonstrates that the HCO_3^- concentration greatly influences the efficiency of electrochemical CO_2 reduction.[30] The enhancement in CO currents and decline in CO FEs might be due to the enhanced interfacial CO_2 concentration and more favorable HER kinetics in the higher concentrated $KHCO_3$ media.[46,49] Accordingly, Fe-N/CNT@GNR-2 achieved a CO current of 22.6 mA cm^{-2} with a CO FE of more than 95% at −0.76 V. Because the single-atom Fe site is considered as the catalytic center for CO_2RR,[10,22] we further sought to improve CO_2RR activity by adding a supernumerary Fe source. However, the catalyst decorated with additional 5 wt % Fe showed much poorer CO FEs as compared to the pristine one, especially at more negative potential ranges (Figure S19a). The EXAFS result suggests that Fe-based particles were formed when adding additional 5 wt % Fe in Fe-N/CNT@GNR (Figure S19b), which explains the poor CO selectivity since Fe-based particles are highly active for hydrogen evolution instead of CO_2 reduction.[46] The results

https://dx.doi.org/10.1021/acsnano.9b09658
ACS Nano 2020, 14, 5506−5516

suggest that Fe-N/CNT@GNR could not stabilize additional Fe atoms to make them atomically dispersed on the CNT@GNR support, probably owing to the limited anchoring sites (defects, N dopants).[10] This is different from a previous work that reported the synthesis of a very high amount of single-atom Ni (20 wt %) on CNTs by pyrolyzing the mixture of Ni, N, and C precursors,[50] in which the formation of single Ni was accompanied by the growth of CNT simultaneously. Note that, although Fe-N/CNT@GNR possessed a relatively low Fe amount (1.75 wt %), it showed a top-level CO_2RR performance in the Fe-N/C community (Table S4), which is even comparable to the state-of-the-art Ni-N/C and Co-N/C, further highlighting the significance of the CNT@GNR network architecture in CO_2RR electrocatalysis.

Stability is another key factor determining the feasibility for practical application. Herein, Fe-N/CNT@GNR-2 can preserve the electrochemical performance in both currents and CO FEs during 5 h continuous CO_2 reduction (Figure 4f), indicating enhanced durability. After long-term electrolysis, the spent catalyst was characterized. The TEM image and XRD pattern show that the spent catalyst preserved its original morphology and carbon crystallinity (Figure S20). The HAADF-STEM image further confirms the dispersion of isolated Fe atoms (Figure 5a), and elemental mapping images demonstrate the

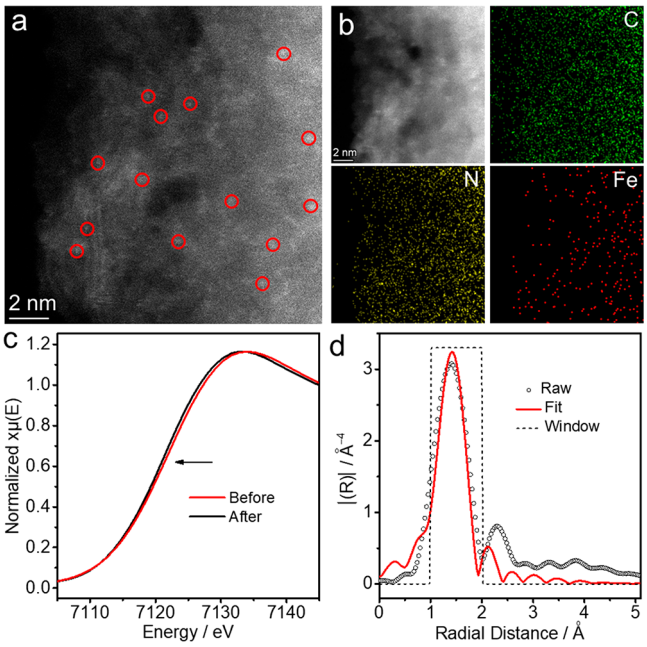

Figure 5. (a) HAADF-STEM and (b) EDS mapping images of Fe-N/CNT@GNR-2 after CO_2 reduction in 0.1 M $KHCO_3$. (c) XANES spectra of Fe-N/CNT@GNR-2 before and after CO_2 reduction. (e) Fourier transformation of EXAFS spectra for spent Fe-N/CNT@GNR-2.

existence of N and Fe species in the carbon matrix (Figure 5b). We further carried out XAS to probe the changes in the chemical states and coordination environment of Fe. XANES spectra show that there was a slight shift to lower energy after electrolysis (Figure 5c), suggesting that no significant change in the Fe oxidization state happened during the CO_2RR process. In a previous study by Hu *et al.*,[45] it was discovered that Fe^{3+} could be reduced to Fe^{2+} at an applied potential more negative than −0.55 V *vs* RHE, which potentially makes Fe-N/C catalysts unstable. In the case of our Fe-N/CNT@GNR, the Fe oxidization state is mostly 2+, as confirmed by XANES (Figure 3d), which might be the reason for the enhanced stability observed here. In addition, the fitting of EXAFS indicates the retention of Fe−N_4 structure (Figure 5d). A similar phenomenon has been observed on atomically dispersed Ni−N_x catalysts for CO_2 reduction.[8,23] The enhanced stability of the Fe−N_4 structure can be ascribed to the strong interaction between Fe atoms with coordinated N atoms and the carbon support, which provides stabilizing effects to anchor single-atom Fe−N_4 species.[20,51,52] However, extensive efforts are still highly needed to explore the underlying stability mechanisms for Fe-N/C catalysts in future research.

In M-N/C, there exist both N dopants and M−N_x species. Previous findings show that "metal-free" N-doped carbon (N-C) materials are active for reducing CO_2 to CO, and active sites in N-C are considered to be pyridinic N, pyrrolic N, and graphitic N.[53−55] However, N-C commonly exhibits much poorer performance (low FE and small partial current density) than counterparts of single-atom M-N/C (Table S5). These reported results strongly suggest that single-atom M−N_x species in M-N/C function as the key, highly efficient catalytic sites in CO_2RR, and N dopants make a minor contribution to CO_2RR. To further reveal the roles of N and Fe in Fe-N/C for CO_2RR, we prepared four representative catalysts using the graphene oxide as the starting material *via* a similar approach (Figure S21), including Fe-N/C, N-C, N-free Fe-containing carbon (Fe-C), and Fe,N-free carbon (C). Fe-N/C showed a maximum CO FE of 80% and a partial current density of 2.1 mA cm^{-2} at an overpotential of 470 mV, which are significantly higher than those of Fe-free N-C (55%, 0.41 mA cm^{-2}) at the same overpotential. Also, it was found that N-free Fe-C and Fe,N-free C exhibited CO FEs less than 1% and partial current density below 0.01 mA cm^{-2} in the whole potential range, but produced H_2 instead. Similarly, the N-free Fe-containing CNT is inactive for CO_2RR too (Figure S1d), indicating the inert nature of pristine carbon toward CO_2RR and the necessity of introducing N and Fe to transform pristine carbon to CO_2RR-active catalysts. It can be thus concluded that both Fe and N are imperative for developing high-performance carbon-based catalysts for CO_2RR. The main role of N is to create N dopants and Fe−N as catalytic species, and Fe−N serves as the principal active site with significantly more enhanced intrinsic reactivity than N dopants for reducing CO_2 to CO.

To gain further mechanistic insight into the catalytic nature of Fe−N_4 moieties, DFT calculations were performed. In our experiments, the typical catalysts studied are Fe-N/CNT, Fe-N/CNT@GNR, and Fe-N/GNR. In Fe-N/CNT, it only has a CNT framework to host atomic Fe−N_4 sites. In Fe-N/CNT@GNR, it has four locations to host Fe−N_4 sites, including the CNT, the GNR bulk plane, GNR armchair edges, and GNR zigzag edges (Figure 6a). In Fe-N/GNR, it has three locations to host Fe−N_4 sites, namely, the GNR bulk plane, GNR armchair edges, and GNR zigzag edges. Therefore, we proposed four models of CNT-Fe−N_4, GNR bulk-Fe−N_4, GNR armchair-Fe−N_4, and GNR zigzag-Fe−N_4 moieties in DFT calculations (Figure S22), which covers all possible active sites in the experimental catalysts.

Assuming that the CO_2RR pathway is a two-step proton-coupled electron transfer process including the formation of intermediates *COOH and *CO and desorption of CO, the Fe atom of the Fe−N_4 complex is regarded as the adsorption site to bind the intermediates.[10,56,57] The optimized adsorption configurations for *COOH and *CO are shown in Figure 6b

https://dx.doi.org/10.1021/acsnano.9b09658
ACS Nano 2020, 14, 5506−5516

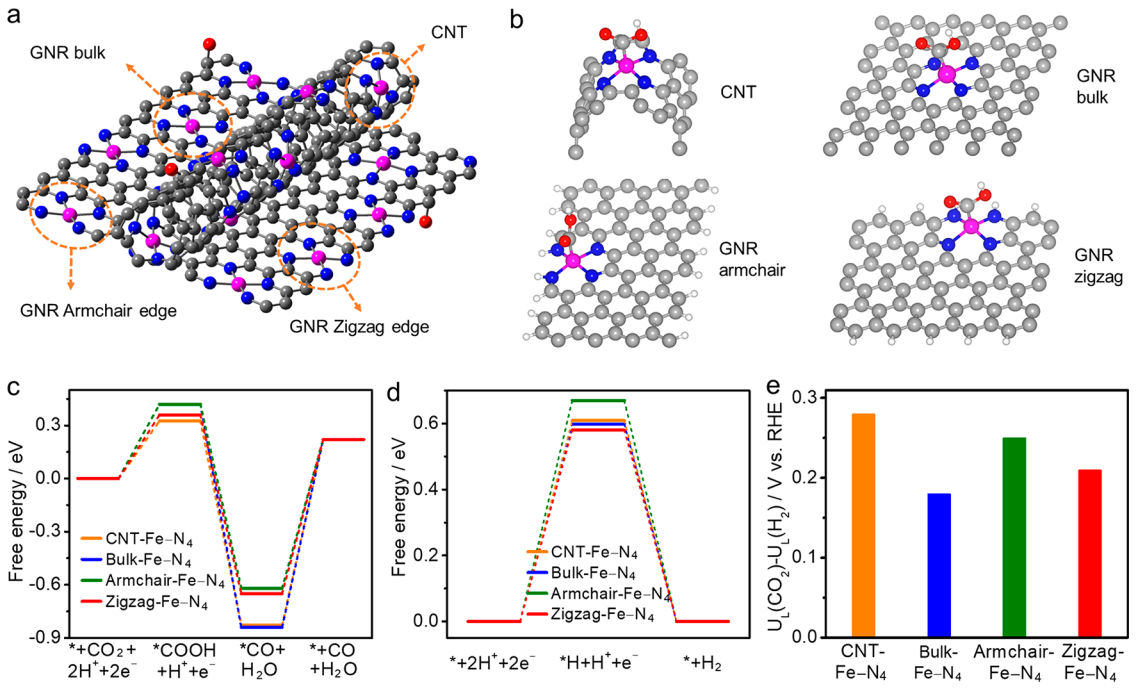

Figure 6. (a) Schematic showing location sites of Fe-N/CNT@GNR to host Fe−N_4 moieties. (b) Atomistic structure of the optimized configurations of *COOH on different sites. (c) Free-energy profiles for CO_2RR. (d) Free-energy profiles for HER. (e) Calculated limiting potential difference between CO_2RR and HER for various moieties. In the figure, the gray, blue, purple, and white balls represent C, N, Fe, and H atoms, respectively.

and Figure S23. From the free energy evolution diagram (Figure 6c), one can see that the CNT site shows a free energy barrier of 0.32 eV for the *COOH formation, lower than that of the GNR zigzag (0.36 eV), GNR bulk (0.42 eV), and GNR armchair sites (0.42 eV). Furthermore, the CO adsorption energy on both armchair and zigzag edges is about 0.3 eV weaker than that on the CNT and GNR bulk sites, suggesting an easier CO desorption on the edge-located sites as compared to the CNT and graphene basal plane sites. We also computed the free energy evolution of the competitive hydrogen evolution to gauge CO_2 reduction selectivity (Figure 6d). The difference between the limiting potentials for CO_2 reduction and H_2 evolution ($U_L(CO_2) - U_L(H_2)$) was calculated, where a positive $U_L(CO_2) - U_L(H_2)$ value corresponds to a good selectivity of CO_2RR.[58] As shown in Figure 6e, all models exhibit positive $U_L(CO_2) - U_L(H_2)$ values, indicating the enhanced capability to suppress HER and thus favor CO_2 reduction on all these proposed moieties. These theoretical findings manifest that the local carbon structure plays a key role in determining the catalytic nature of Fe−N_4 sites toward CO_2 reduction.

In the CO_2 reduction, there are two potential-related steps: the formation of *COOH and *CO (Figure 6c). The former is a thermodynamically uphill process at 0 V, while the later is thermodynamically downhill. Thus, the formation of *COOH is the potential-limiting step in the CO_2 reduction process. The theoretical limiting potential (U_L), corresponding to the onset potential in the experiment, is the most positive potential to overcome the free energy barrier and make all potential-related steps downhill, such as −0.33 V on CNT-Fe−N_4 (Figure S24). Therefore, an ideal site for CO_2 reduction is expected to have a low free energy barrier for *COOH formation for enabling a positive limiting potential and thus a small overpotential. In addition, a weak CO adsorption and a positive $U_L(CO_2) - U_L(H_2)$ value are also necessary to afford a large production rate (partial current) and maintain a high FE for CO_2 reduction, respectively. As for Fe-N/CNT, although the CNT-Fe−N_4 site is good for CO_2 activation and HER suppression, the presence of Fe particles may reduce the catalytic CO_2RR activity and selectivity since previous studies have demonstrated that carbon-encapsulated iron nanoparticles favor hydrogen evolution over CO_2 reduction,[46,59] which explains the most negative onset potential (−0.5 V) and lowest CO FE (82%) on Fe-N/CNT among the series catalysts. In the case of Fe-N/CNT@GNR-2, it possessed monodispersed Fe−N_4 sites at both CNT and GNR bulk and edges; the CNT and zigzag sites could promote CO_2 activation, and the zigzag and armchair edges could weaken CO adsorption. Together with the largest electrochemical active area and sufficient mass transfer, Fe-N/CNT@GNR-2 was thus able to deliver an improved CO_2 reduction performance with the most positive onset potential (−0.3 V), highest CO FE (98%), and largest CO partial current (22.6 mA cm^{-2} at −0.76 V) than others. Regarding Fe-N/GNR, it had the highest portion of the GNR bulk site with the unfavorable *COOH formation/CO desorption and low electrochemical active area, which collectively results in a relatively poor CO_2RR activity as compared to Fe-N/CNT@GNR-2 but better than Fe-N/CNT (Figure 4b,c). As for Fe-N/CNT@GNR-1, it has a structure closer to Fe-N/CNT due to limited unzipping of CNT, whereas the structure of Fe-N/CNT@GNR-3 is very analogous to Fe-N@GNR owing to the absence of the majority of CNT. Because the CO_2RR activity is largely dependent on the structure of catalysts, it can be inferred that the catalytic CO_2RR behaviors of Fe-N/CNT@GNR-1 might be similar to that of Fe-N/CNT, while Fe-N/CNT@GNR-3 performs very closely to Fe-N/GNR. Thereby, the structure differences might result in the observed activity tendency, following the order Fe-N/CNT@GNR-1 < Fe-N/CNT@GNR-3 < Fe-N/CNT@GNR-2. All these findings

https://dx.doi.org/10.1021/acsnano.9b09658
ACS Nano 2020, 14, 5506−5516

highlight that both single-atom Fe sites and the carbon support structure are of great importance in boosting CO_2 reduction, which are suggested to be engineered collectively in order to reach an enhanced CO_2RR performance.

CONCLUSIONS

In summary, we demonstrated the facile transformation of commercial CNTs into efficient CO_2 reduction catalysts featuring atomically dispersed Fe sites on hierarchical carbon nanotube and graphene nanoribbon networks. The mesoporous CNT@GNR architecture enables both a highly electrochemically active surface area and rapid mass transport. The nanostructure also contains isolated Fe−N_4 centers supported on the CNT and GNR basal plane and edge sites for CO_2 activation with suppressed hydrogen evolution, as revealed by DFT computations. Benefiting from the high intrinsic reactivity and selectivity of atomic Fe−N_4 and optimal carbon mesostructure, Fe-N/CNT@GNR exhibited improved activity toward CO_2 reduction, achieving a stable CO FE of 96% and a partial current of 22.6 mA cm^{-2} at −0.76 V *vs* RHE, one of the highest results among reported activities on M-N/C catalysts. This work suggests a viable method of synthesizing single-atom metal catalysts directly from earth-abundant materials at a large scale. Moreover, it reveals the significance of support structure in governing the intrinsic reactivity and physical properties of atomic catalysts.

METHODS

Catalysts Synthesis. Raw multiwalled CNTs (Cheap Tubes Nanomaterials) were treated in concentrated HCl for 24 h for further use. In a typical synthesis, CNTs (500 mg) were dispersed in concentrated H_2SO_4 (100 mL), sonicated for 1 h, and stirred for 4 h. Then, a certain amount of $KMnO_4$ was slowly added and stirred for 1 h. The mixture was heated in an oil bath at 55 °C for 30 min; the temperature was further increased to 70 °C and kept there for 10 min. After the mixture was cooled to room temperature, it was poured into ice water (200 mL) containing 30 wt % H_2O_2 (10 mL). The mixture was centrifuged and washed with 15 wt % HCl five times and ethanol two times and dried in a vacuum oven overnight. The structure evolution was controlled by adjusting the $KMnO_4$:CNTs mass ratio from 0, 1, 2, 3, to 4, respectively, and the corresponding oxidized samples were named O/CNT, O/CNT@GNR-1, O/CNT@GNR-2, O/CNT@GNR-3, and O/GNR. Heating the mixture of oxidized samples and urea with a mass ratio of 1:20 at 900 °C for 1 h generates the final catalysts, named Fe-N/CNT, Fe-N/CNT@GNR-1, Fe-N/CNT@GNR-2, Fe-N/CNT@GNR-3, and Fe-N/GNR. Among these catalysts, Fe-N/CNT@GNR-2 showed the highest performance, which thus refers to Fe-N/CNT@GNR.

Catalyst Characterization. HAADF-STEM (FEI 200 kV Titan Themis), TEM (FEI Tecnai G2 F20 ST), XPS (Omicron), and XRD (Bruker D8) were performed to characterize the morphology, structure, and composition of as-prepared catalysts. Metal amounts were determined by ICP-MS (PerkinElmer NexION 300D Quadrupole). A Micromeritics ASAP 2420 physisorption analyzer was used to conduct BET analyses. XAS was collected at the bending magnet station, 12-BM at the Advanced Photon Source at Argonne National Lab. Fluorescence data was collected at room temperature at the Fe K-edge (7112 eV) using a 13-element germanium detector. Data were processed and fitted using the Athena and Artemis programs as part of the Demeter software package.

Electrochemical Measurements. CO_2RR performance of catalysts and control samples was measured using a three-electrode system in a two-chamber cell separated by an ion exchange membrane (Nafion 115). The CO_2-saturated $KHCO_3$ aqueous solutions (0.1, 0.5, and 1.0 M) were used as electrolytes. To prepare the working electrode, catalyst powder (3 mg) was dispersed in a mixture solution of ethanol (370 μL), DI water (200 μL), and 5% Nafion solution (30 μL) under sonication for 3 h. The ink was then dropped on a piece of carbon paper with a mass loading of 0.8 mg cm^{-2}, which acts as the working electrode, and was placed in the cathode chamber. An Ag/AgCl (3 M KCl) and a Pt foil were used as the reference electrode and counter electrode, which were placed in the cathode chamber and anode chamber, respectively. The CO_2 was delivered to the cathode chamber at a flow rate of 34 mL min^{-1} for 1 h before electrolysis and was kept there during measurements. The recorded potentials after *iR* compensation were rescaled to the reversible hydrogen electrode (RHE). The concentration of gaseous products was measured by an online gas chromatograph (Fuel Cell GC-2014ATF, Shimadzu), which is equipped with a methanizer-assisted flame ionization detector and a thermal conductivity detector. ^{1}H NMR was employed to detect liquid-phase products.

Faradaic efficiency of products was calculated based on the equation

$$\mathrm{FE} = \frac{zPFVv_i}{RTJ}$$

where z is the number of transferred electrons, P is the pressure (1.01×10^5 Pa), F is the Faraday constant (96500 C mol^{-1}), V is the volumetric flow rate of CO_2 (5.67×10^{-7} m^3 s^{-1}), v_i is the volumetric concentration of gaseous product, R is the gas constant (8.314 J mol^{-1} K^{-1}), T is the room temperature (298.15 K), and J is the steady-state current.

DFT Calculations. The Vienna *ab initio* simulation package was used to perform spin-polarized DFT calculations. The core electrons were described by a projector augmented wave pseudopotential. To expand the wave functions, the cutoff energy was set to 400 eV. The electronic exchange and correlation were described by the generalized gradient approximation of the Perdew−Burke−Ernzernhof functionals. Four Fe−N_4 moieties with different carbon structure were proposed as CO_2RR active sites. Specifically, a (5,5) SWCNT was used to model the CNT-Fe−N_4 site, a periodic graphene layer with 64 carbon atoms was used to model the GNR bulk-Fe−N_4, a H-terminated graphene ribbon with 64 carbon atoms was used to model the GNR armchair-Fe−N_4 site, and a H-terminated graphene ribbon with 60 carbon atoms was used to model the GNR zigzag-Fe−N_4 site. The $1 \times 1 \times 5$, $3 \times 3 \times 1$, $1 \times 3 \times 1$, $3 \times 1 \times 1$, and $1 \times 3 \times 1$ Monkhorst-pack *k*-point meshes were employed to sample the Brillouin zone for the CNT and GNR bulk, GNR armchair, and GNR zigzag active sites, respectively. The optimization of atomic positions was carried out until the force fell below 0.01 eV/Å.

The free energy of CO_2RR was calculated by the equation below:

$$\Delta G = \Delta E_{\mathrm{DFT}} + \Delta E_{\mathrm{ZPE}} + \Delta E_{\mathrm{solv}} + \Delta H - T\Delta S$$

where ΔE_{DFT}, ΔE_{ZPE}, ΔE_{solv}, ΔH, and ΔS are the energy change, zero-point energy correction, solvation energy correction, reaction enthalpy change, and reaction entropy change. The solvation corrections for the stabilization of *COOH and *CO were 0.25 and 0.1 eV, respectively.

ASSOCIATED CONTENT

Supporting Information

The Supporting Information is available free of charge at https://pubs.acs.org/doi/10.1021/acsnano.9b09658.

Additional characterization results for catalysts' structure and composition, electrochemical CO_2 reduction performance, theoretical DFT calculations, and activity comparison tables (PDF)

AUTHOR INFORMATION

Corresponding Author

Ying Li − *J. Mike Walker '66 Department of Mechanical Engineering, Texas A&M University, College Station, Texas 77843, United States;* orcid.org/0000-0002-6775-5649; Email: yingli@tamu.edu

https://dx.doi.org/10.1021/acsnano.9b09658
ACS Nano 2020, 14, 5506−5516

Authors

Fuping Pan − *J. Mike Walker '66 Department of Mechanical Engineering, Texas A&M University, College Station, Texas 77843, United States;* orcid.org/0000-0001-9171-0726

Boyang Li − *Department of Mechanical Engineering and Materials Science, University of Pittsburgh, Pittsburgh, Pennsylvania 15261, United States*

Erik Sarnello − *Department of Chemistry and Biochemistry, Northern Illinois University, DeKalb, Illinois 60115, United States*

Yuhuan Fei − *Department of Materials Science and Engineering, Michigan Technological University, Houghton, Michigan 49931, United States*

Yang Gang − *J. Mike Walker '66 Department of Mechanical Engineering, Texas A&M University, College Station, Texas 77843, United States*

Xianmei Xiang − *J. Mike Walker '66 Department of Mechanical Engineering, Texas A&M University, College Station, Texas 77843, United States*

Zichen Du − *J. Mike Walker '66 Department of Mechanical Engineering, Texas A&M University, College Station, Texas 77843, United States*

Peng Zhang − *Department of Chemistry, Texas A&M University, College Station, Texas 77843, United States;* orcid.org/0000-0003-0973-1523

Guofeng Wang − *Department of Mechanical Engineering and Materials Science, University of Pittsburgh, Pittsburgh, Pennsylvania 15261, United States;* orcid.org/0000-0001-8249-4101

Hoai T. Nguyen − *Department of Chemistry and Biochemistry, Northern Illinois University, DeKalb, Illinois 60115, United States*

Tao Li − *Department of Chemistry and Biochemistry, Northern Illinois University, DeKalb, Illinois 60115, United States; Chemistry and Material Science Group, X-ray Science Division, Argonne National Laboratory, Lemont, Illinois 60439, United States*

Yun Hang Hu − *Department of Materials Science and Engineering, Michigan Technological University, Houghton, Michigan 49931, United States*

Hong-Cai Zhou − *Department of Chemistry, Texas A&M University, College Station, Texas 77843, United States;* orcid.org/0000-0002-9029-3788

Complete contact information is available at: https://pubs.acs.org/10.1021/acsnano.9b09658

Notes

The authors declare no competing financial interest.

ACKNOWLEDGMENTS

This work was supported by U.S. National Science Foundation (NSF CBET #1805132, NSF CBET #1804534, NSF CMMI #1661699) and American Chemical Society Petroleum Research Fund (ACS-PRF, #58167-ND10). T.L. is thankful for the support from NIU startup. The authors acknowledge the use of Advanced Photon Source, an Office of Science User Facility operated for the U.S. Department of Energy (DOE) Office of Science by Argonne National Laboratory supported by the U.S. DOE under Contract DE-AC02-06CH11357, the computational resources provided by the University of Pittsburgh Center for Research Computing and the Extreme Science and Engineering Discovery Environment (XSEDE) supported by U.S. NSF ACI-1053575, and the Materials Characterization Facility at Texas A&M University.

REFERENCES

(1) De Luna, P.; Hahn, C.; Higgins, D.; Jaffer, S. A.; Jaramillo, T. F.; Sargent, E. H. What Would It Take for Renewably Powered Electrosynthesis to Displace Petrochemical Processes? *Science* **2019**, *364*, 3506.

(2) Bushuyev, O. S.; De Luna, P.; Dinh, C. T.; Tao, L.; Saur, G.; Van De Lagemaat, J.; Kelley, S. O.; Sargent, E. H. What Should We Make with CO_2 and How Can We Make It? *Joule* **2018**, *2*, 825−832.

(3) Gao, S.; Lin, Y.; Jiao, X.; Sun, Y.; Luo, Q.; Zhang, W.; Li, D.; Yang, J.; Xie, Y. Partially Oxidized Atomic Cobalt Layers for Carbon Dioxide Electroreduction to Liquid Fuel. *Nature* **2016**, *529*, 68−71.

(4) Li, J.; Chen, G.; Zhu, Y.; Liang, Z.; Pei, A.; Wu, C.-L.; Wang, H.; Lee, H. R.; Liu, K.; Chu, S.; Cui, Y. Efficient Electrocatalytic CO_2 Reduction on a Three-Phase Interface. *Nat. Catal.* **2018**, *1*, 592−600.

(5) Lu, Q.; Jiao, F. Electrochemical CO_2 Reduction: Electrocatalyst, Reaction Mechanism, and Process Engineering. *Nano Energy* **2016**, *29*, 439−456.

(6) Chen, Y.; Li, C. W.; Kanan, M. W. Aqueous CO_2 Reduction at Very Low Overpotential on Oxide-Derived Au Nanoparticles. *J. Am. Chem. Soc.* **2012**, *134*, 19969−19972.

(7) Lu, Q.; Rosen, J.; Zhou, Y.; Hutchings, G. S.; Kimmel, Y. C.; Chen, J. G.; Jiao, F. A Selective and Efficient Electrocatalyst for Carbon Dioxide Reduction. *Nat. Commun.* **2014**, *5*, 3242.

(8) Yang, H. B.; Hung, S.-F.; Liu, S.; Yuan, K.; Miao, S.; Zhang, L.; Huang, X.; Wang, H.-Y.; Cai, W.; Chen, R.; Gao, J.; Yang, X.; Chen, W.; Huang, Y.; Chen, H. M.; Li, C. M.; Zhang, T.; Liu, B. Atomically Dispersed Ni(i) As the Active Site for Electrochemical CO_2 Reduction. *Nat. Energy* **2018**, *3*, 140−147.

(9) Yan, C.; Li, H.; Ye, Y.; Wu, H.; Cai, F.; Si, R.; Xiao, J.; Miao, S.; Xie, S.; Yang, F.; Li, Y.; Wang, G.; Bao, X. Coordinatively Unsaturated Nickel-Nitrogen Sites towards Selective and High-Rate CO_2 Electroreduction. *Energy Environ. Sci.* **2018**, *11*, 1204−1210.

(10) Bi, W.; Li, X.; You, R.; Chen, M.; Yuan, R.; Huang, W.; Wu, X.; Chu, W.; Wu, C.; Xie, Y. Surface Immobilization of Transition Metal Ions on Nitrogen-Doped Graphene Realizing High-Efficient and Selective CO_2 Reduction. *Adv. Mater.* **2018**, *30*, 1706617.

(11) Varela, A. S.; Kroschel, M.; Leonard, N. D.; Ju, W.; Steinberg, J.; Bagger, A.; Rossmeisl, J.; Strasser, P. pH Effects on the Selectivity of the Electrocatalytic CO_2 Reduction on Graphene-Embedded Fe-N-C Motifs: Bridging Concepts between Molecular Homogeneous and Solid-State Heterogeneous Catalysis. *ACS Energy Lett.* **2018**, *3*, 812−817.

(12) Wang, X.; Chen, Z.; Zhao, X.; Yao, T.; Chen, W.; You, R.; Zhao, C.; Wu, G.; Wang, J.; Huang, W.; Yang, J.; Hong, X.; Wei, S.; Wu, Y.; Li, Y. Regulation of Coordination Number over Single Co Sites: Triggering the Efficient Electroreduction of CO_2. *Angew. Chem., Int. Ed.* **2018**, *57*, 1944−148.

(13) Pan, Y.; Lin, R.; Chen, Y.; Liu, S.; Zhu, W.; Cao, X.; Chen, W.; Wu, K.; Cheong, W.-C.; Wang, Y. Design of Single-Atom Co-N_5 Catalytic Site: A Robust Electrocatalyst for CO_2 Reduction with Nearly 100% CO Selectivity and Remarkable Stability. *J. Am. Chem. Soc.* **2018**, *140*, 4218−4221.

(14) Cheng, Y.; Zhao, S.; Li, H.; He, S.; Veder, J.-P.; Johannessen, B.; Xiao, J.; Lu, S.; Pan, J.; Chisholm, M. F.; Yang, S. Z.; Liu, C.; Chen, J. G.; Jiang, S. P. Unsaturated Edge-Anchored Ni Single Atoms on Porous Microwave Exfoliated Graphene Oxide for Electrochemical CO_2. *Appl. Catal., B* **2019**, *243*, 294−303.

(15) Pan, F.; Deng, W.; Justiniano, C.; Li, Y. Identification of Champion Transition Metals Centers in Metal and Nitrogen-Codoped Carbon Catalysts for CO_2 Reduction. *Appl. Catal., B* **2018**, *226*, 463−472.

(16) Pan, F.; Zhang, H.; Liu, Z.; Cullen, D.; Liu, K.; More, K.; Wu, G.; Wang, G.; Li, Y. Atomic-Level Active Sites of Efficient Imidazolate Framework-Derived Nickel Catalysts for CO_2 Reduction. *J. Mater. Chem. A* **2019**, *7*, 26231−26237.

(17) Lu, C.; Yang, J.; Wei, S.; Bi, S.; Xia, Y.; Chen, M.; Hou, Y.; Qiu, M.; Yuan, C.; Su, Y.; Zhang, F.; Liang, H.; Zhuang, X. Atomic Ni Anchored Covalent Triazine Framework As High Efficient Electrocatalyst for Carbon Dioxide Conversion. *Adv. Funct. Mater.* **2019**, *29*, 1806884.
(18) Pan, F.; Zhao, H.; Deng, W.; Feng, X.; Li, Y. A Novel N,Fe-Decorated Carbon Nanotube/Carbon Nanosheet Architecture for Efficient CO_2 Reduction. *Electrochim. Acta* **2018**, *273*, 154−161.
(19) Cheng, N.; Stambula, S.; Wang, D.; Banis, M. N.; Liu, J.; Riese, A.; Xiao, B.; Li, R.; Sham, T.-K.; Liu, L.-M.; Botton, G. A.; Sun, X. Platinum Single-Atom and Cluster Catalysis of the Hydrogen Evolution Reaction. *Nat. Commun.* **2016**, *7*, 13638.
(20) Wan, X.; Liu, X.; Li, Y.; Yu, R.; Zheng, L.; Yan, W.; Wang, H.; Xu, M.; Shui, J. Fe-N-C Electrocatalyst with Dense Active Sites and Efficient Mass Transport for High-Performance Proton Exchange Membrane Fuel Cells. *Nat. Catal.* **2019**, *2*, 259−268.
(21) Pan, F.; Zhang, H.; Liu, K.; Cullen, D. A.; More, K. L.; Wang, M.; Feng, Z.; Wang, G.; Wu, G.; Li, Y. Unveiling Active Sites of CO_2 Reduction on Nitrogen Coordinated and Atomically Dispersed Iron and Cobalt Catalysts. *ACS Catal.* **2018**, *8*, 3116−3122.
(22) Zhang, C.; Yang, S.; Wu, J.; Liu, M.; Yazdi, S.; Ren, M.; Sha, J.; Zhong, J.; Nie, K.; Jalilov, A. S.; Li, Z.; Li, H.; Yakobson, B. I.; Wu, Q.; Ringe, E.; Xu, H.; Ajayan, P. M.; Tour, J. M. Electrochemical CO_2 Reduction with Atomic Iron-Dispersed on Nitrogen-Doped Graphene. *Adv. Energy Mater.* **2018**, *8*, 1703487.
(23) Zheng, T.; Jiang, K.; Ta, N.; Hu, Y.; Zeng, J.; Liu, J.; Wang, H. Large-Scale and Highly Selective CO_2 Electrocatalytic Reduction on Nickel Single-Atom Catalyst. *Joule* **2019**, *3*, 265−278.
(24) Hu, B.-C.; Wu, Z.-Y.; Chu, S.-Q.; Zhu, H.-W.; Liang, H.-W.; Zhang, J.; Yu, S.-H. SiO_2-Protected Shell Mediated Templating Synthesis of Fe-N-Doped Carbon Nanofibers and Their Enhanced Oxygen Reduction Reaction Performance. *Energy Environ. Sci.* **2018**, *11*, 2208−2215.
(25) Sa, Y. J.; Seo, D.-J.; Woo, J.; Lim, J. T.; Cheon, J. Y.; Yang, S. Y.; Lee, J. M.; Kang, D.; Shin, T. J.; Shin, H. S.; Jeong, H. Y.; Kim, C. S.; Kim, M. G.; Kim, T.-Y.; Joo, S. H. A General Approach to Preferential Formation of Active Fe−N_x Sites in Fe-N/C Electrocatalysts for Efficient Oxygen Reduction Reaction. *J. Am. Chem. Soc.* **2016**, *138*, 15046−15056.
(26) Tang, C.; Wang, H.-F.; Zhang, Q. Multiscale Principles to Boost Reactivity in Gas-Involving Energy Electrocatalysis. *Acc. Chem. Res.* **2018**, *51*, 881−889.
(27) Georgakilas, V.; Tiwari, J. N.; Kemp, K. C.; Perman, J. A.; Bourlinos, A. B.; Kim, K. S.; Zboril, R. Noncovalent Functionalization of Graphene and Graphene Oxide for Energy Materials, Biosensing, Catalytic, and Biomedical Applications. *Chem. Rev.* **2016**, *116*, 5464−5519.
(28) Sun, H.; Mei, L.; Liang, J.; Zhao, Z.; Lee, C.; Fei, H.; Ding, M.; Lau, J.; Li, M.; Wang, C.; Xu, X.; Hao, G.; Papandrea, B.; Shakir, I.; Dunn, B.; Huang, Y.; Duan, X. Three-Dimensional Holey-Graphene/Niobia Composite Architectures for Ultrahigh-Rate Energy Storage. *Science* **2017**, *356*, 599−604.
(29) Liang, Y.; Wang, H.; Zhou, J.; Li, Y.; Wang, J.; Regier, T.; Dai, H. Covalent Hybrid of Spinel Manganese-Cobalt Oxide and Graphene As Advanced Oxygen Reduction Electrocatalysts. *J. Am. Chem. Soc.* **2012**, *134*, 3517−3523.
(30) Zhao, C.; Wang, Y.; Li, Z.; Chen, W.; Xu, Q.; He, D.; Xi, D.; Zhang, Q.; Yuan, T.; Qu, Y.; Yang, J.; Zhou, F.; Yang, Z.; Wang, X.; Wang, J.; Luo, J.; Li, Y.; Duan, H.; Wu, Y.; Li, Y. Solid-Diffusion Synthesis of Single-Atom Catalysts Directly from Bulk Metal for Efficient CO_2 Reduction. *Joule* **2019**, *3*, 584−594.
(31) Kosynkin, D. V.; Higginbotham, A. L.; Sinitskii, A.; Lomeda, J. R.; Dimiev, A.; Price, B. K.; Tour, J. M. Longitudinal Unzipping of Carbon Nanotubes to Form Graphene Nanoribbons. *Nature* **2009**, *458*, 872.
(32) Rangel, N. L.; Sotelo, J. C.; Seminario, J. M. Mechanism of Carbon Nanotubes Unzipping into Graphene Ribbons. *J. Chem. Phys.* **2009**, *131*, No. 031105.
(33) Li, J.-L.; Kudin, K. N.; McAllister, M. J.; Prud'homme, R. K.; Aksay, I. A.; Car, R. Oxygen-Driven Unzipping of Graphitic Materials. *Phys. Rev. Lett.* **2006**, *96*, 176101.
(34) Hu, H.; Guan, B.; Xia, B.; Lou, X. W. Designed Formation of Co_3O_4/$NiCo_2O_4$ Double-Shelled Nanocages with Enhanced Pseudocapacitive and Electrocatalytic Properties. *J. Am. Chem. Soc.* **2015**, *137*, 5590−5595.
(35) Lee, S. H.; Kim, J.; Chung, D. Y.; Yoo, J. M.; Lee, H. S.; Kim, M. J.; Mun, B. S.; Kwon, S. G.; Sung, Y.-E.; Hyeon, T. Design Principle of Fe-N-C Electrocatalysts: How to Optimize Multimodal Porous Structures? *J. Am. Chem. Soc.* **2019**, *141*, 2035−2045.
(36) Li, X.; Wang, H.; Robinson, J. T.; Sanchez, H.; Diankov, G.; Dai, H. Simultaneous Nitrogen Doping and Reduction of Graphene Oxide. *J. Am. Chem. Soc.* **2009**, *131*, 15939−15944.
(37) Arrigo, R.; Schuster, M. E.; Xie, Z.; Yi, Y.; Wowsnick, G.; Sun, L. L.; Hermann, K. E.; Friedrich, M.; Kast, P.; Hävecker, M.; Knop-Gericke, A.; Schlögl, R. Nature of the N−Pd Interaction in Nitrogen-Doped Carbon Nanotube Catalysts. *ACS Catal.* **2015**, *5*, 2740−2753.
(38) Arrigo, R.; Schuster, M. E. On the High Structural Heterogeneity of Fe-Impregnated Graphitic-Carbon Catalysts from Fe Nitrate Precursor. *Catalysts* **2019**, *9*, 303.
(39) Pan, F.; Li, B.; Sarnello, E.; Hwang, S.; Gang, Y.; Feng, X.; Xiang, X.; Adli, N. M.; Li, T.; Su, D.; Wu, G.; Wang, G.; Li, Y. Boosting CO_2 Reduction on Fe-N-C with Sulfur Incorporation: Synergistic Electronic and Structural Engineering. *Nano Energy* **2020**, *68*, 104384.
(40) Hou, S.; Cai, X.; Wu, H.; Yu, X.; Peng, M.; Yan, K.; Zou, D. Nitrogen-Doped Graphene for Dye-Sensitized Solar Cells and the Role of Nitrogen States in Triiodide Reduction. *Energy Environ. Sci.* **2013**, *6*, 3356−3362.
(41) Zhang, J.; Zhao, Y.; Chen, C.; Huang, Y.-C.; Dong, C.-L.; Chen, C.-J.; Liu, R.-S.; Wang, C.; Yan, K.; Li, Y.; Wang, G. Tuning the Coordination Environment in Single-Atom Catalysts to Achieve Highly Efficient Oxygen Reduction Reactions. *J. Am. Chem. Soc.* **2019**, *141*, 20118−20126.
(42) Zitolo, A.; Goellner, V.; Armel, V.; Sougrati, M.-T.; Mineva, T.; Stievano, L.; Fonda, E.; Jaouen, F. Identification of Catalytic Sites for Oxygen Reduction in Iron- and Nitrogen-Doped Graphene Materials. *Nat. Mater.* **2015**, *14*, 937−942.
(43) Chen, Y.; Ji, S.; Wang, Y.; Dong, J.; Chen, W.; Li, Z.; Shen, R.; Zheng, L.; Zhuang, Z.; Wang, D.; Li, Y. Isolated Single Iron Atoms Anchored on N-Doped Porous Carbon As an Efficient Electrocatalyst for the Oxygen Reduction Reaction. *Angew. Chem., Int. Ed.* **2017**, *56*, 1−6.
(44) Fei, H.; Dong, J.; Feng, Y.; Allen, C. S.; Wan, C.; Volosskiy, B.; Li, M.; Zhao, Z.; Wang, Y.; Sun, H.; An, P.; Chen, W.; Guo, Z.; Lee, C.; Chen, D.; Shakir, I.; Liu, M.; Hu, T.; Li, Y.; Kirkland, A. I.; et al. General Synthesis and Definitive Structural Identification of MN_4C_4 Single-Atom Catalysts with Tunable Electrocatalytic Activities. *Nat. Catal.* **2018**, *1*, 63−72.
(45) Gu, J.; Hsu, C.-S.; Bai, L.; Chen, H. M.; Hu, X. Atomically Dispersed Fe^{3+} Sites Catalyze Efficient CO_2 Electroreduction to CO. *Science* **2019**, *364*, 1091−1094.
(46) Huan, T. N.; Ranjbar, N.; Rousse, G.; Sougrati, M.; Zitolo, A.; Mougel, V.; Jaouen, F.; Fontecave, M. Electrochemical Reduction of CO_2 Catalyzed by Fe-N-C Materials: A Structure−Selectivity Study. *ACS Catal.* **2017**, *7*, 1520−1525.
(47) Nitopi, S.; Bertheussen, E.; Scott, S. B.; Liu, X.; Engstfeld, A. K.; Horch, S.; Seger, B.; Stephens, I. E. L.; Chan, K.; Hahn, C.; Nørskov, J. K.; Jaramillo, T. F.; Chorkendorff, I. Progress and Perspectives of Electrochemical CO_2 Reduction on Copper in Aqueous Electrolyte. *Chem. Rev.* **2019**, *119*, 7610−7672.
(48) Ross, M. B.; De Luna, P.; Li, Y.; Dinh, C.-T.; Kim, D.; Yang, P.; Sargent, E. H. Designing Materials for Electrochemical Carbon Dioxide Recycling. *Nat. Catal.* **2019**, *2*, 648−658.
(49) Wuttig, A.; Yaguchi, M.; Motobayashi, K.; Osawa, M.; Surendranath, Y. Inhibited Proton Transfer Enhances Au-Catalyzed CO_2-to-Fuels Selectivity. *Proc. Natl. Acad. Sci. U. S. A.* **2016**, *113*, E4585−E4593.

https://dx.doi.org/10.1021/acsnano.9b09658
ACS Nano 2020, 14, 5506−5516

(50) Cheng, Y.; Zhao, S. Y.; Johannessen, B.; Veder, J.-P.; Saunders, M.; Rowles, M. R.; Cheng, M.; Liu, C.; Chisholm, M. F.; Marco, R. D.; Cheng, H. M.; Yang, S. Z.; Jiang, S. P. Atomically Dispersed Transition Metals on Carbon Nanotubes with Ultrahigh Loading for Selective Electrochemical Carbon Dioxide Reduction. *Adv. Mater.* **2018**, *30*, 1706287.
(51) Chung, H. T.; Cullen, D. A.; Higgins, D.; Sneed, B. T.; Holby, E. F.; More, K. L.; Zelenay, P. Direct Atomic-Level Insight into the Active Sites of a High-Performance PGM-Free ORR Catalyst. *Science* **2017**, *357*, 479−484.
(52) Genovese, C.; Schuster, M. E.; Gibson, E. K.; Gianolio, D.; Posligua, V.; Grau-Crespo, R.; Cibin, G.; Wells, P. P.; Garai, D.; Solokha, V.; Calderon, K. S.; Velasco-Velez, J. J.; Ampelli, C.; Perathoner, S.; Held, G.; Centi, G.; Arrigo, R. Operando Spectroscopy Study of the Carbon Dioxide Electro-Reduction by Iron Species on Nitrogen-Doped Carbon. *Nat. Commun.* **2018**, *9*, 935.
(53) Cui, X.; Pan, Z.; Zhang, L.; Peng, H.; Zheng, G. Selective Etching of Nitrogen-Doped Carbon by Steam for Enhanced Electrochemical CO_2 Reduction. *Adv. Energy Mater.* **2017**, *7*, 1701456.
(54) Xu, J.; Kan, Y.; Huang, R.; Zhang, B.; Wang, B.; Wu, K.-H.; Lin, Y.; Sun, X.; Li, Q.; Centi, G.; Su, D. Revealing the Origin of Activity in Nitrogen-Doped Nanocarbons towards Electrocatalytic Reduction of Carbon Dioxide. *ChemSusChem* **2016**, *9*, 1085−1089.
(55) Wu, J.; Liu, M.; Sharma, P. P.; Yadav, R. M.; Ma, L.; Yang, Y.; Zou, X.; Zhou, X.-D.; Vajtai, R.; Yakobson, B. I.; Lou, J.; Ajayan, P. M. Incorporation of Nitrogen Defects for Efficient Reduction of CO_2 *via* Two-Electron Pathway on Three-Dimensional Graphene Foam. *Nano Lett.* **2016**, *16*, 466−470.
(56) Asadi, M.; Kim, K.; Liu, C.; Addepalli, A. V.; Abbasi, P.; Yasaei, P.; Phillips, P.; Behranginia, A.; Cerrato, J. M.; Haasch, R.; Zapol, P.; Kumar, B.; Klie, R. F.; Abiade, J.; Curtiss, L. A.; Salehi-Khojin, A. Nanostructured Transition Metal Dichalcogenide Electrocatalysts for CO_2 Reduction in Ionic Liquid. *Science* **2016**, *353*, 467−470.
(57) Ju, W.; Bagger, A.; Hao, G.-P.; Varela, A. S.; Sinev, I.; Bon, V.; Roldan Cuenya, B.; Kaskel, S.; Rossmeisl, J.; Strasser, P. Understanding Activity and Selectivity of Metal-Nitrogen-Doped Carbon Catalysts for Electrochemical Reduction of CO_2. *Nat. Commun.* **2017**, *8*, 944.
(58) Pan, F.; Li, B.; Xiang, X.; Wang, G.; Li, Y. Efficient CO_2 Electroreduction by Highly Dense and Active Pyridinic Nitrogen on Holey Carbon Layers with Fluorine Engineering. *ACS Catal.* **2019**, *9*, 2124−2133.
(59) Tavakkoli, M.; Kallio, T.; Reynaud, O.; Nasibulin, A. G.; Johans, C.; Sainio, J.; Jiang, H.; Kauppinen, E. I.; Laasonen, K. Single-Shell Carbon-Encapsulated Iron Nanoparticles: Synthesis and High Electrocatalytic Activity for Hydrogen Evolution Reaction. *Angew. Chem., Int. Ed.* **2015**, *54*, 4535−4538.

https://dx.doi.org/10.1021/acsnano.9b09658
ACS Nano 2020, 14, 5506−5516